# Improved Tentacle-Based Guidance for Reentry Gliding Hypersonic Vehicle With No-Fly Zone Constraint

**YANG GAO** [ID] [1], **GUANGBIN CAI** [1,2], **XIAOGANG YANG** [1], **AND MINGZHE HOU** [3]

[1] College of Missile Engineering, Rocket Force University of Engineering, Xi'an 710025, China
[2] School of Astronautics, Northwestern Polytechnical University, Xi'an 710072, China
[3] School of Astronautics, Harbin Institute of Technology, Harbin 150080, China

Corresponding author: Guangbin Cai (cgb0712@163.com)

**ABSTRACT** An improved tentacle-based bank-angle transient method that requires less computation and provides effective feedback is proposed to offer a new choice for reentry gliding hypersonic vehicle maneuvering guidance. The longitudinal guidance strategy of hypersonic vehicles is applied to track standard trajectories, and the improved tentacle-based bank angle transient lateral strategy avoids static or dynamic no-fly zones. The proposed lateral strategy generates three tentacles for detection, addresses numerical heading angle limitations or no-fly zone constraints, and provides control commands through a time-counting filter. Dispersed cases are verified for static no-fly zones, and a warning area is proposed to avoid dynamic no-fly zones. For dynamic no-fly zones, the velocity and initial position of the no-fly zone are discussed in terms of the impact on the guidance. Finally, the guidance strategy is tested on a high-performance Common Aero Vehicle model in many flights, and all results for the constraints and computation time indicate that the improved tentacle-based guidance method is effective for avoiding no-fly zones where some information is unknown.

## I. INTRODUCTION

In recent decades, guidance studies on the reentry of hypersonic vehicles have been extensively conducted to develop the aerospace industry among the world's great powers [1]–[11]. During the reentry of a hypersonic vehicle, multiple constraints must be satisfied. In a previous study, guidance generally considered two types of constraints: path constraints and position-restriction constraints.

Path constraints include the heating rate, the aerodynamic load, and the dynamic pressure. The design of off-line trajectory optimization has been applied these constraints and many achievements have been obtained, and there is an irreversible trend from off-line computing to online computing for trajectory optimization [12]–[16]. The pseudo-spectral method is representative of methods applied in off-line trajectory optimization, with adaptive meshes increasing the convergence

rate of the results, calculating relatively precise discrete results off-line [13], [14]. In many experiments, the more accurate the trajectory is, the longer the calculation time is, which cannot meet the requirements of online application. To apply a precise track to the standard trajectory online, profiles such as drag-energy, drag-speed, and altitude-speed have been proposed [17]–[19]. Later, the velocity-altitude-azimuth profile method was proposed and applied to achieve a controllable and reachable flight corridor [20]. The main purpose of these methods is tracking, but with new constraints added, such as no-fly zones and waypoint constraints, they lose their online applicability.

The second type of constraint is the position-restriction constraint in the form of longitude and latitude, such as waypoints and no-fly zones. A waypoint is a condition constraint that the vehicle must go through in the flight process, whereas the no-fly zone is an area that the vehicle cannot enter; waypoints can also be used to avoid no-fly zones [21], [22]. By identifying the shape of the no-fly zone,

the waypoints are studied and designed, and the trajectory optimization results of the segments are obtained quickly if the whole trajectory has been divided by the waypoints from the first. Therefore, most of the current research studies the trajectory optimization algorithm in the case of no-fly zones or waypoints with absolutely known information [21]. A no-fly zone usually has information including shape, velocity, and position. However, the velocity of a no-fly zone is usually considered as zero, but if the vehicle faces the no-fly zone with unknown information or with information that changes during the flight, such a method will be no longer applicable to the vehicle maneuvering guidance.

A tentacle-based method is a new way to solve the online trajectory calculation when the constraints are complicated. After studying the tentacle feedback mechanism of insect biology, it is proposed to use fewer "tentacles" to detect the situation in the unknown area ahead and to get feedback, and then provide control commands [23]–[25]. The tentacle-based method was first proposed in research on the path-planning of mobile robots, where the tentacles are the possible movement direction of the robot. A maneuvering guidance strategy based on two tentacles is applied in hypersonic vehicles [26], where two tentacles are continuously generated forward to obtain feedback and to implement reversal control of the bank angle to avoid the no-fly zone without specific information. However, this method is not mature for three reasons. First, this method lacks forward path detection, and thus the vehicle always turns left or right to avoid all constraints through the method of threat evaluation, even when the vehicle is flying without any obstacles ahead. The bank angle makes the vehicle sway from side to side but there is no rationale for doing so, which increases the complexity of guidance and flight distance. Second, in the feedback from the tentacles, empirical data is used for the heading angle constraint; however, empirical data may not be suitable for other vehicles or other situations, and thus it is not universally applicable. Third, research on the tentacle-based method has not been carried out in situations of dynamic no-fly zones. In fact, the shape of a no-fly zone changes and is more likely to be composed of multiple small areas to form a composite area, and the method is not suitable for this situation. Seeing that the detection distance of a mobile robot is relatively short, so that many tentacles can be generated. However, a hypersonic gliding vehicle could not have many detection tentacles, which significantly increases both the detection time and the complexity of the control system, because the number of tentacles is the same as the types of lateral guidance control command.

In this paper, a bank angle transient guidance strategy based on improved tentacle detection is proposed. The vehicle generates tentacles with left, middle, and right directions, and the feedback of each tentacle is limited by five cases, namely, time constraint, path constraints, no-fly zone constraint, heading angle constraint, and stop condition. In the design of the lateral guidance, only three bank angles are adopted to avoid no-fly zones in the lateral guidance, whereas

a linear quadratic regulator algorithm is adopted to track the velocity and position of the original standard trajectory in the longitudinal guidance. The improved tentacle-based method guidance strategy described in this paper is also a model predictive control (MPC) approach [27], which has three advantages. First, the tentacle detection of the forward path is added, and a time-counting filter is adopted to reduce the transverse of the bank angle, which gives more non-maneuvering flight time and reduces the airframe load. Second, the computed heading angle constraint is proposed to reduce the dependence on empirical data for other vehicles. Third, the influence of the initial position and velocity of the dynamic no-fly zone on the maneuvering guidance strategy is studied, which has never been explored. The effectiveness of the guidance strategy is verified on a high-performance common aero vehicle (CAV-H) by different missions with static and dynamic no-fly zones.

## II. REENTRY MODELING
### A. DYNAMICS MODELING FOR HYPERSONIC GLIDE VEHICLE REENTRY
The three-dimensional point-mass dynamics of an entry vehicle over a rotating spherical Earth are given by [28]. To simplify the model, the rotational angular velocity of the earth is ignored and the formulas are as follows:

$$\dot{r} = V \sin \gamma \tag{1}$$
$$\dot{\theta} = V \cos \gamma \sin \psi / r \cos \varphi \tag{2}$$
$$\dot{\varphi} = V \cos \gamma \cos \psi / r \tag{3}$$
$$\dot{V} = -D/m - g \sin \gamma \tag{4}$$
$$\dot{\gamma} = 1/V[L \cos \sigma / m + \left(V^2/r - g\right) \cos \gamma] \tag{5}$$
$$\dot{\psi} = 1/V[L \sin \sigma / m \cos \gamma + V^2 \cos \gamma \sin \psi \tan \varphi / r] \tag{6}$$

where $r$ is the radial distance from the center of the Earth to the vehicle, $V$ is the Earth-relative velocity, $\gamma$ is the flight-path angle, $\theta$ is the longitude, $\varphi$ is the latitude, $\psi$ is the velocity heading angle, and $\sigma$ is the bank angle. The terms $D$ and $L$ are the aerodynamic drag and lift forces, respectively, which are $D = \rho V^2 S_{ref} C_D / 2$ and $L = \rho V^2 S_{ref} C_L / 2$, where $\rho$ is the atmospheric density and $S_{ref}$ is the reference area of the vehicle. Further, $D$ and $L$ are functions of $\alpha$, the angle of attack, through the dependence of drag and lift coefficients $C_D$ and $C_L$.

### B. TRAJECTORY CONSTRAINTS
Typical reentry trajectory inequality constraints include heating rate, aerodynamic load, and dynamic pressure, as shown in formulas (7), (8), and (9) [29]:

$$Q = K_Q \rho^{0.5} V^{3.15} \leq Q_{\max} \tag{7}$$
$$n = \sqrt{L^2 + D^2}/m \leq n_{\max} \tag{8}$$
$$\bar{q} = 0.5 \rho V^2 \leq \bar{q}_{\max} \tag{9}$$

where $Q_{\max}$, $n_{\max}$, and $\bar{q}_{\max}$ are maximum limits for these constraints, respectively. Formula (7) is the heating rate constraint at a specified point on the surface of the vehicle, with

$K_Q = 7.9686 \times 10^{-5}$ Js/$^2$(m$^{3.5}$kg$^{0.5}$). Moreover, given an initial condition, the reentry vehicle is expected to reach a terminal area with a terminal state that consists of $[r_f \quad V_f \quad \gamma_f]$.

Apart from the typical inequality constraints and terminal constraints mentioned above, no-fly zones need to be considered in many missions. For a general case, the no-fly zone constraint is expressed as

$$\min \left\{ S_N^1, S_N^2, S_N^3, \cdots S_N^n \right\} \geq 0 \tag{10}$$

where $n$ is the number of no-fly zones and the distance $S_N^i$ ($1 \leq i \leq n$) is measured from the vehicle to the nearest boundary of the $i$th zone, as shown in Fig. 1. There are static and dynamic no-fly zones in fact, and the dynamic ones are usually smaller than the static ones.
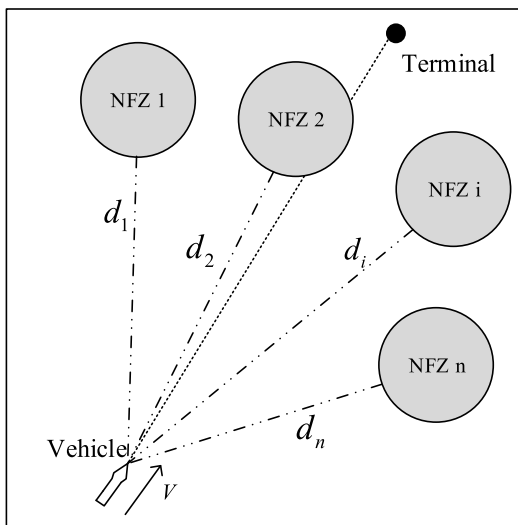


**FIGURE 1. Distances between vehicle and no-fly zones.**

## C. NUMERICAL HEADING ANGLE CONSTRAINT

To detect the situation ahead, the vehicle needs to predict a few trajectories, which are called tentacles. The tentacles should be stopped by some conditions, such as no-fly zone constraints and time constraints. In addition to these constraints, the heading angle constraint can limit the tentacles from making excessive turns. The heading angle constraint is related to the velocity of the vehicle in many experiments; for example, [26] provides a set of empirical data as shown in Fig. 2. Such empirical data is feasible for some no-fly zones, but they are not universally applicable for other vehicles. Therefore, a computed method is needed to give the constraint of heading angle.

First, to get the relationship between the velocity of the vehicle and heading angle constraint, a maximum turn trajectory is computed as shown in Fig. 3. The heading angle error $\Psi_i$ is the inner angle between the direction of the velocity and the direction from the real-time position of the vehicle ($\theta_i, \phi_i$) to the terminal point $C$ ($\theta_C, \phi_C$).
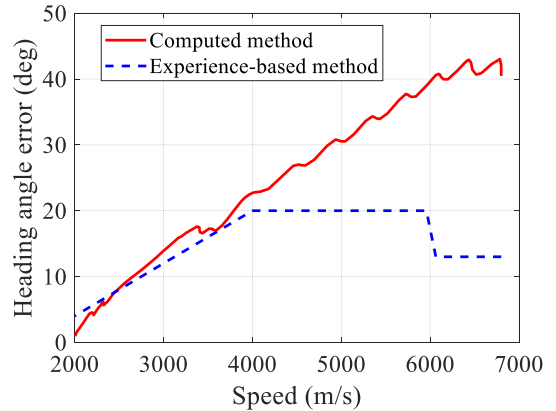


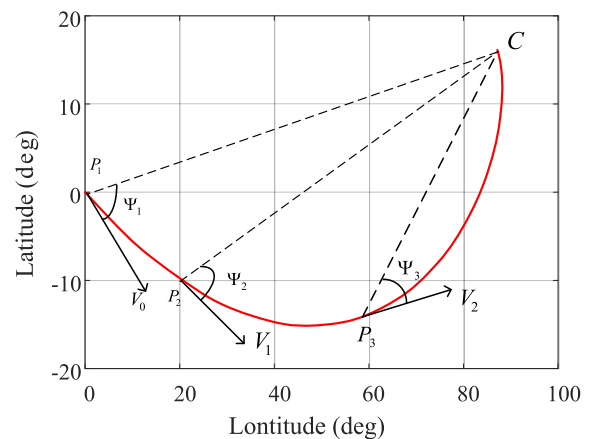**FIGURE 2. Experienced-based and numerical heading angle constraint.**



**FIGURE 3. Maximum turn trajectory and the heading angle with speed.**

Second, $\Psi_i$ is computed by:

$$\Psi_i = \psi_i - \arctan\left(\frac{\theta_C - \theta_i}{\phi_C - \phi_i}\right) \tag{11}$$

where the $[\psi_i, \theta_i, \phi_i]$ is the heading angle, longitude, and latitude, respectively, of the $i$th point, such as the points $[P_1, P_2, P_3, \cdots, C]$.

Finally, the difference between the computed and experience-based methods is shown as a solid line and dotted lines in Fig. 2. When the velocity is more than 4, 000 m/s, the computed method gives the vehicle more opportunities to turn with a larger bank angle to avoid obstacles. When the velocity is less than 4, 000 m/s, the results are roughly the same. Therefore, the computed method will be more practical for the maneuvering guidance of vehicle.

## III. BANK ANGLE TRANSIENT GUIDANCE STRATEGY BASED ON IMPROVED TENTACLE DETECTION

### A. BASIC GUIDANCE STRATEGY WITH WAYPOINTS

For trajectory tracking, the guidance strategy is divided into the longitudinal guidance strategy and the lateral guidance strategy. The longitudinal one is designed by the linear quadratic regulator(LQR) on the basis of waypoints. That
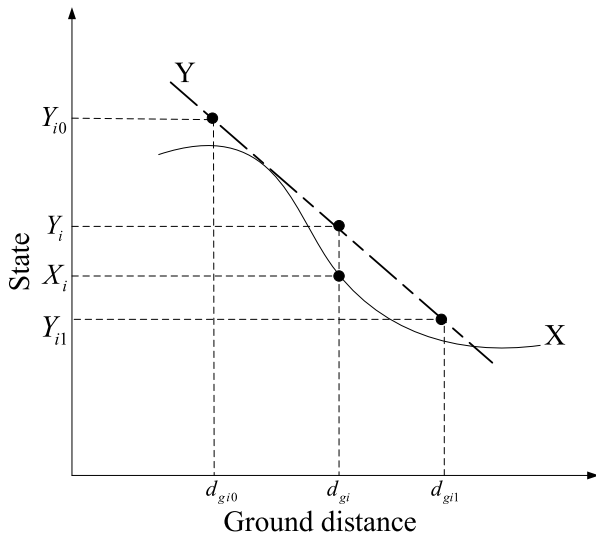
**FIGURE 4.** Linearization of waypoint state at $i$th moment.

is, the actual state at the $(i + 1)$th moment is determined by the actual state and the standard original state with a given bank angle at the $i$th moment. However, because the waypoints of standard trajectory are usually discrete and the intervals between them are random, these waypoints should be linearized to the state $Y_i$ through the ground distance $d_{gi}$ of longitude and latitude to be compared with the real trajectory state $X_i$ at the $i$th moment because the ground distance is always monotonic. Generally, $d_{gi}$ is simplified as the longitude when the latitude changes slightly in the original trajectory. Therefore, the state of the waypoint of each moment can be obtained by linearization of the states of the closer original waypoint as formula (12).

$$Y_i = Y_{i0} + (Y_{i1} - Y_{i0}) \left( d_{gi} - d_{gi0} \right) / \left( d_{gi1} - d_{gi0} \right) \quad (12)$$

As shown in Fig. 4, $Y_i = [r_i, V_i, \gamma_i]$ is the linearized state at the $i$th ground distance, whereas $Y_{i0}$ and $Y_{i1}$ are the original states at two moments before and after, respectively, the $i$th ground distance, and $d_{gi0}$ and $d_{gi1}$ are their ground distances, respectively. Furthermore, the control commands of the original trajectory should be also linearized to calculate $\alpha_i$. The term $X_i$ is the actual state calculated from the $(i - 1)$th moment, and the longitudinal guidance strategy is given by [30], [31]:

$$\Delta\alpha_i = K(s)(X_i - Y_i) \quad (13)$$

where $\Delta\alpha_i$ is an adjustment for the angle of attack along the standard trajectory and $(X_i - Y_i)$ is the difference between the actual trajectory and the standard linearized one, whereas the bank angle $\sigma_i$ should be updated by the lateral guidance during the flight. The term $K(s)$ is determined off-line by the LQR method and computed onboard to track the linearized waypoints of the standard trajectory. Note that the state of waypoints only consists of $[r, V, \theta]$ in formula (13) because the other states of trajectory might be adjusted in the lateral movement [31]. After $\alpha_i$ is obtained from the standard one

and $\Delta\alpha_i$, the actual state at the $(i + 1)$th moment can be obtained and the algorithm goes on.

During the flight, there might be some no-fly zones in front of the vehicle, and the lateral guidance would consider the detected feedback after every update time $\Delta T_{lat}$, which might be more or less. Let $\Delta T_{lon}$ be the update time between the two moments of actual states and the update time of the longitudinal guidance strategy [26]. That is, the relationship of update times at $i$th moment is set as follows:

$$\Delta T_{lat} = \begin{cases} k\Delta T_{lon}, & \sigma_i = \sigma_{i+1} \\ \Delta T_{lon}, & \sigma_i \neq \sigma_{i+1} \end{cases} \quad (14)$$

where $\sigma_i$ and $\sigma_{i+1}$ are the bank angles of the $i$th and $(i + 1)$th moments and parameter $k$ determines the update frequency relationship between the two guidance strategies. When $\Delta T_{lat}$ is larger than $\Delta T_{lon}$, the update frequency of the lateral guidance strategy is less than that of the longitudinal guidance strategy. Otherwise, the two guidance strategies are updated with the same frequency. Note that $k = 1$ is allowed as well when $\sigma_i = \sigma_{i+1}$ to increase the detection effect of the lateral guidance.

### B. TENTACLES PREDICTION

For the constraint of no-fly zone, the tentacles are generated by numerical integration, and it is necessary to get precise feedback and generate a prediction efficiently. The states of the tentacles are propagated numerically by formulas (1–6), whereas the constant changes of $r$ and $\gamma$ are considered [32], [33], which increases the accuracy of trajectory detection and the flight becomes more realistic.

These tentacles have three directions—right, left, and middle—representing positive, negative, and zero bank angles, respectively. That is, each of the three tentacles' trajectories are controlled by a constant bank angle. For each of the tentacles, the angle of attack is designed by longitudinal guidance strategy.

First, as shown in Fig. 5, whatever two or three tentacles generated at the point, the effect and the feedback are the same at points such as point O, because the middle and right tentacles meet the no-fly zone, and thus only the left one can be generated. It is obvious that two tentacles cannot give good feedback when the vehicle flies into points like the $AB$ section, which makes reversal of the bank angle inconvenient. The two tentacles described in [26] would make vehicle swing left and right during flight. In sections such as $AB$, the middle tentacle could finish the generation and make the vehicle go through the terminal place, which would be more effective in cases where the vehicle is caught in the middle. The start of the generation of each tentacle is the moment $i$, where $t = i - \Delta T_{lat}$ is the present time and $\Delta T_{lat}$ is the internal of updating the bank angle. After some improvement of [26], the break conditions are as follows:

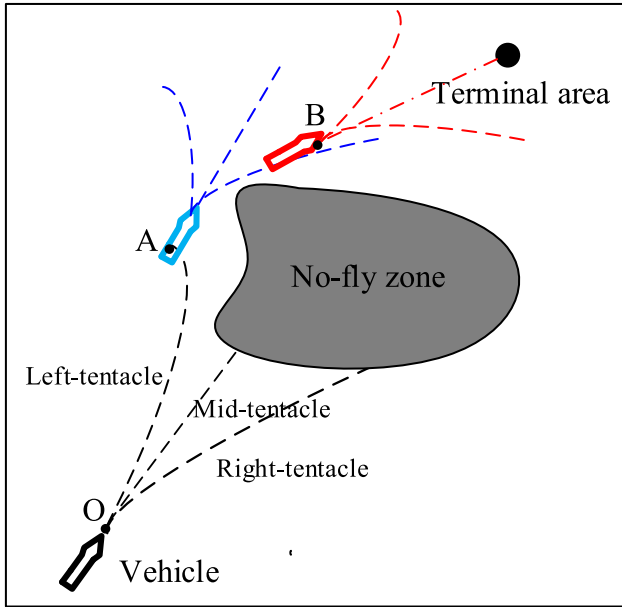*Condition 1*: $t \geq t_{\max}$, which means that the flight time $t$ exceeds its maximum limit;

**FIGURE 5.** Three tentacles at different points.

*Condition 2*: The heating rate, aerodynamic load and dynamic pressure are bigger than their maximum limits;

*Condition 3*: $S_N^i \leq 0 \, (1 \leq i \leq n)$, which means that the vehicle has entered the $i$th no-fly zone;

*Condition 4*: $|\Psi_i| \geq \Psi_{\max}(V)$, which means that the velocity heading angle has deviated too much to make vehicle loss target at the $i$th moment.

*Condition 5*: The vehicle reaches the terminal place.

Among them, conditions 1–4 are restrictive conditions, where the vehicle should avoid flying to the end of these three types of "tentacles." The last termination condition is a permissive condition, and the vehicle should preferentially choose such a "tentacle" to fly. The no-fly zone termination condition is the most restrictive condition, and the time termination condition is less likely to choose; thus, the "tentacle" selection priority $Ka$ corresponding to the termination condition is designed as [2, 2, 10, 5, 1] for conditions 1–5. The termination condition priority $Ka$ will be used to calculate the total bank angle priority and to choose the bank angle at every moment.

## C. LATERAL GUIDANCE METHOD BASED ON BANK ANGLE TRANSIENTS

Lateral guidance gives bank angle commands to the control system of a vehicle, whereas the bank angle should be chosen by the priority calculation and be filtered by the time counting filter.

First, this study designed three tentacles for detection, so there are three options for bank angle in the lateral guidance strategy. Here are the formulas for calculating the priority and the getting the value of symbolic function $sgn(\sigma)$ at $i$th moment:

$$\sigma_i = sgn(\sigma) \cdot \sigma_{\max}, \quad sgn(\sigma) \in \{-1, 0, 1\} \quad (15)$$

$$K_j = -Ka_j \cdot Kb_j, \quad j = Left, Mid, Right \quad (16)$$

$$sgn(\sigma) = \begin{cases} -1, & K_{Left} = \max(K_j) \\ 0, & K_{Mid} = \max(K_j) \\ 1, & K_{Right} = \max(K_j) \end{cases} \quad (17)$$

where $\sigma_{\max}$ is the maximum bank angle, and the left, middle, and right tentacles correspond to $-1$, 0, and 1, respectively, of the symbolic function $sgn(\sigma)$. The assignment of the symbolic function is determined by the total priority $K_j$ of the feedback of the tentacle. The total priority $K_j$ is determined by the termination condition priority $Ka_j$ and the distance priority $Kb_j$ decided by the distances between the end points of the tentacles and the end point. The smaller the distance is, the closer the end position of the tentacle is to the terminal area, the more possible it is that the tentacle would be selected. That is, according to the distance, the three levels are designated separately {1.1, 1.0, 0.9}. The larger the priority $K_j$ is in formula (16), the more representative of the tentacles should be selected as the guidance command for the next moment.

Second, to solve the problem of the vehicle being subjected to a high-frequency change or large oscillation in bank angle when the control system cannot complete such changes due to the priority oscillation variation, the lateral guidance method adopts a time-counting filter after the priority calculating. The result $\sigma_i$ calculated by the bank angle symbol function at the $i$th moment enters the time-counting filter. The filter saves the value and judges as follows:

$$A_c = [\sigma_{i-T_s}, \sigma_{i-T_s+1}, \cdots, \sigma_i], \quad T_s + 1 \leq i \leq t_{\max} \quad (18)$$

$$\sigma_r = \begin{cases} -\sigma_{\max}, & \sum A_c \leq -k_\sigma \sigma_{\max} \\ \sigma_{\max}, & \sum A_c \geq k_\sigma \sigma_{\max} \\ 0, & else \end{cases} \quad (19)$$

where $A_c$ is the bank angle of consecutive moments during $T_s$, $T_s$ is the number of cumulative moments, $\sigma_r$ is the final output at the $i$th moment, and the coefficient $k_\sigma$ is one-third of $T_s$. When the moment is less than the $(T_s + 1)$th moment, the time-counting filter is not deployed because the bank angle is chosen as the angle at the first moment.

## D. WARNING-AREA MODELING FOR DYNAMIC NO-FLY ZONES

When the vehicle is facing a dynamic no-fly zone, if the vehicle views the dynamic no-fly zone as a static zone, the vehicle will not calculate the influence of the velocity in the no-fly zone during the flight. When the vehicle is approaching the dynamic no-fly zone where the no-fly zone is moving toward the vehicle, the vehicle will crash it into if the no-fly zone catches the vehicle, even though the vehicle successfully chooses to avoid the "static" no-fly zone before the crash. Therefore, the vehicle needs to detect some movement information of the no-fly zone using its tentacles as much as possible. However, the tentacles can only touch the no-fly points at the end, and the specific shape and velocity of the no-fly zone cannot be known by any of the tentacles.

First, the judgment of the static and the dynamic no-fly zone can be detected by the six tentacle detection lines of the previous and current prediction; that is, the tentacles generated at the $i$th moment and the $(i + 1)$th moment, as shown in Fig. 6. When any of the previous tentacles generated at the $i$th moment encounter the no-fly zone again at the $(i + 1)$th moment, it is concluded that the no-fly zone has moved. As shown in Fig. 6, when the time is at the $i$th moment, the left tentacle of the vehicle encounters the no-fly zone at point A, and at the next moment, the new tentacle of the same direction encounters the dynamic no-fly zone at point C after the movement of the no-fly zone, and the previous tentacle meets the moved no-fly zone at point B. Owing to the left tentacle generated at the $i$th moment meets the no-fly zone at two points, this no-fly zone detected by the left tentacle is judged to be a dynamic no-fly zone.



**FIGURE 7.** The strike of dynamic no-fly zone in two cases.



**FIGURE 6.** Detection for dynamic no-fly zone.
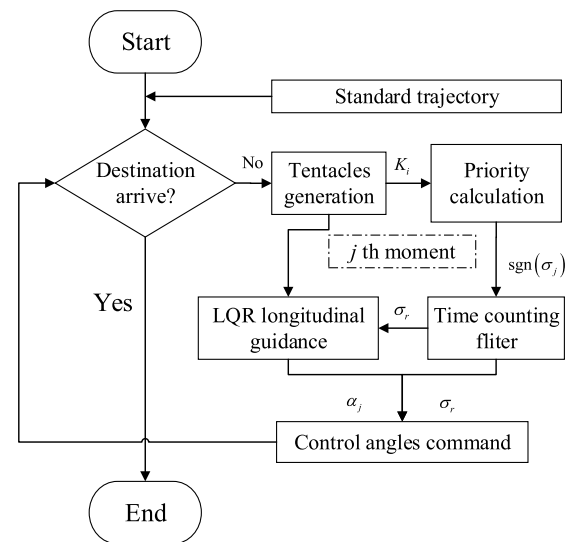


**FIGURE 8.** Algorithm flowchart including longitudinal and lateral guidance.

Secondly, a warning area radiating from point C is put forward because the direction of $V_N$ and the radius of the dynamic no-fly zone is unknown. When the vehicle avoids a static no-fly zone, the vehicle usually chooses the better trajectory through the edge of the static no-fly zone that is blocking its original trajectory. However, the dynamic no-fly zone may move toward the vehicle as vehicle approaches the zone. If two of the three tentacles of the vehicle have encountered the no-fly zone as shown in Fig.7(a), whether this zone is static or dynamic, the vehicle will choose another tentacle without a no-fly zone according to the priority calculation. As shown in Fig.7(b), if only one tentacle meets the dynamic no-fly zone, the vehicle should start avoidance at that moment. In this case, the control system adjusts $\sigma$ to the maximum, and the vehicle should choose the tentacle in either the left or the right direction to avoid the no-fly zone until it is no longer detected. Considering the real-time point C detected in the no-fly zone as the center and a gradual increase in the radius $R_C$, the warning area expands. Until the second
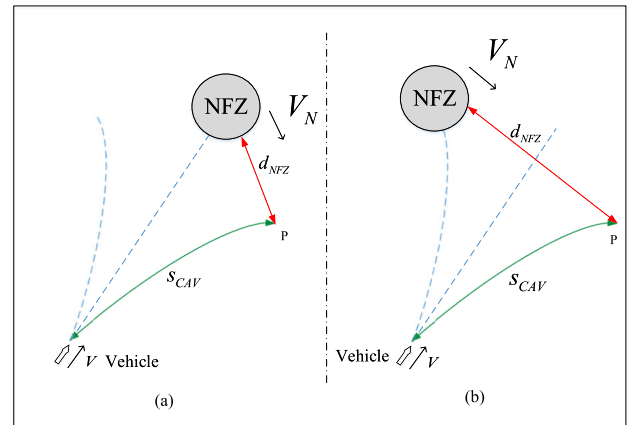
of the three tentacles meets in the warning area, the vehicle would choose another tentacle without meeting a no-fly zone or warning area. As shown in Fig. 7, the vehicle should fly to point P through the distance $s_{CAV}$ before the dynamic no-fly zone moves over the distance $d_{NFZ}$. If the initial position of the dynamic no-fly zone is close enough or its velocity is fast enough, it is difficult for the vehicle to avoid it.

## IV. NUMERICAL RESULTS
The CAV-H model is used to verify the improved tentacle-based guidance strategy, whose dry weight and reference are 907.2 kg and 0.484 m$^2$, respectively. The database of the lift coefficients, the drag coefficients, and the lift-to-drag ratio can be found in [34]. As the CAV-H achieves its maximum lift-to-drag ratio with the angle of attack being 10 deg, the standard trajectory is designed with the attack angle ranging from 10 deg to 15 deg. The main parameters used in the testing are listed in Table 1:

**TABLE 1.** Initial and terminal conditions of standard flight.

| Parameters | Initial | $3\sigma$ | Terminal |
|---|---|---|---|
| Altitude, km | 70 | 1 | 30 |
| Velocity, m/s | 6800 | 50 | 2000 |
| Flight-path angle, deg | 0 | 0.3 | $[-90, 90]$ |
| Lontitude, deg | 2 | 0.3 | 96 |
| Latitude, deg | 0 | 1 | 0 |
| Heading angle, deg | 90 | 1 | $[0, 180]$ |
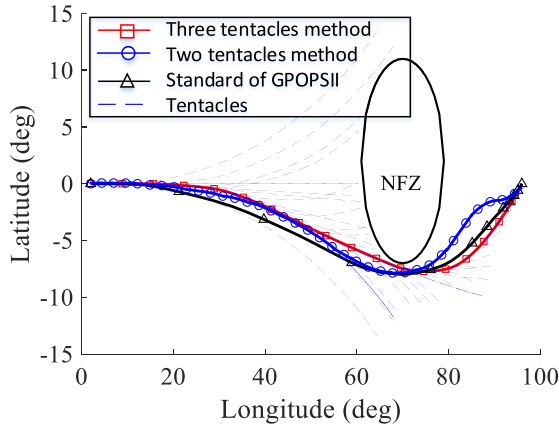


**FIGURE 9.** Ground guidance for circle no-fly zone.



**FIGURE 10.** Ground guidance for rectangle no-fly zone.



**FIGURE 11.** Ground guidance for double rectangular channel no-fly zone.



**FIGURE 12.** Ground guidance for sinusoidal channel no-fly zone.

In Table 1, the dispersions for the initial condition are given in the third column. The path constraints are $Q_{max} = 4$ MW/m$^2$, $n_{max} = 2.5$ g, and $\bar{q}_{max} = 60$ kPa. The maximum flight time is $t_{max} = 3000$ s, with the guidance cycle update time $\Delta T_{lon} = \Delta T_{lat} = 1$ s. The data and the standard trajectory are used to do conventional and discrete simulations under static no-fly zones and dynamic no-fly zones according to the algorithm flowchart shown in Fig.8.

Five missions are considered in this study to verify the effectiveness of the improved strategy and the advantages compared with the method in [26]. Missions 1 and 2 are single no-fly zones, such as circular and rectangular no-fly zones. Missions 3 and 4 are complex multiple no-fly zones, such that the CAV-H can only fly through the narrow channels. Furthermore, mission 5 has a dynamic no-fly zone, which increases the difficulty of guidance. Furthermore, dispersed cases are verified for four static missions, and the influence of initial position and velocity of dynamic no-fly zones are discussed. Last, the path constraints and computational performance of all trajectories are verified.

### A. STATIC NO-FLY ZONE CASES

The guidance method is verified first in missions 1–4 in the conventional cases of static no-fly zones. They are circular, rectangular, double rectangular, and sinusoidal channel no-fly zones. The vehicles' tracks with no-fly zones are showed in Figs. 9–12. In these figures, the red solid trajectories are the ones made by the improved maneuvering guidance strategy with three tentacles in every guidance update cycle, and the blue dotted ones are the tentacles drawn every 100 s. The
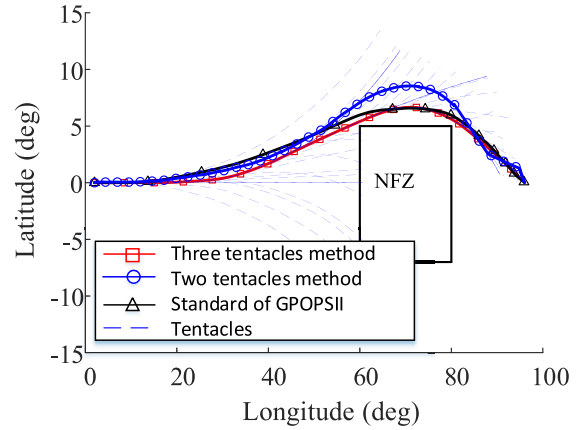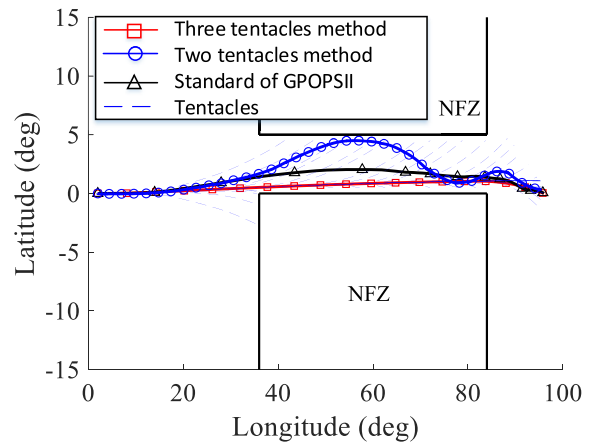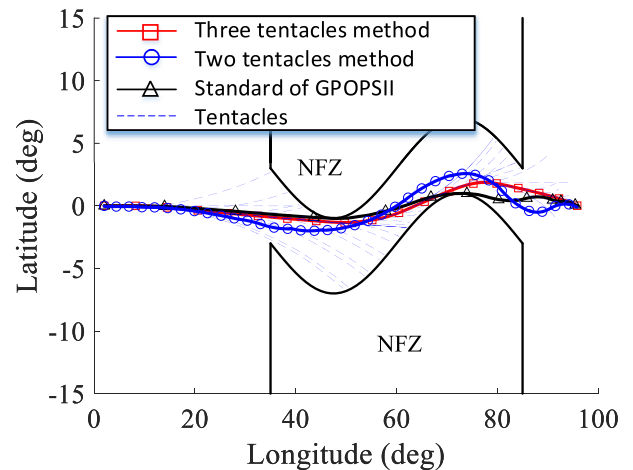
blue solid trajectories are the results from [26], made by the bank angle reversal strategy model based on double-tentacle detection. The black solid trajectories are figured using the GPOPS II toolkit. For example, mission 1 shows a vehicle that flies to the terminal place with a circular no-fly zone
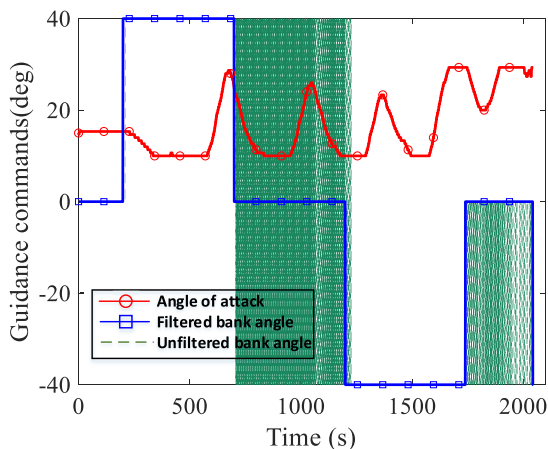
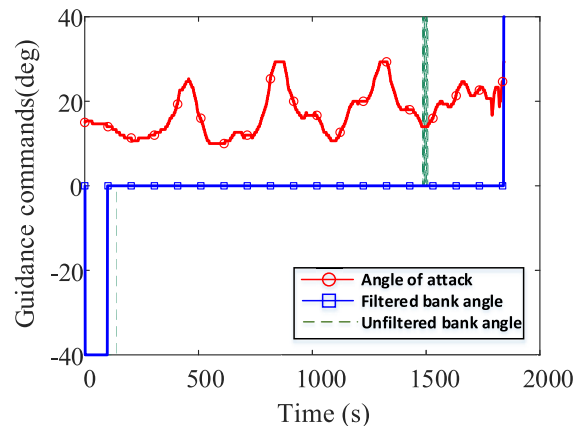**FIGURE 13.** Control commands for circular no-fly zone.



**FIGURE 15.** Control commands for double rectangular channel no-fly zone.
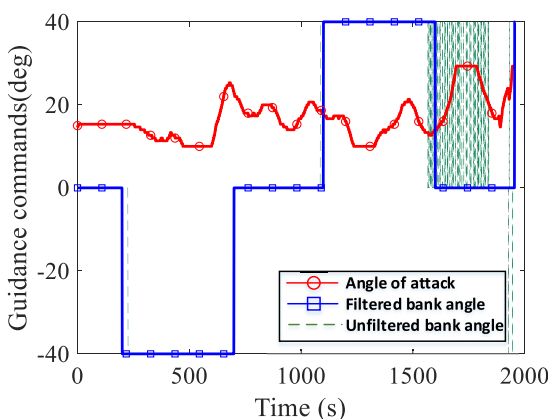


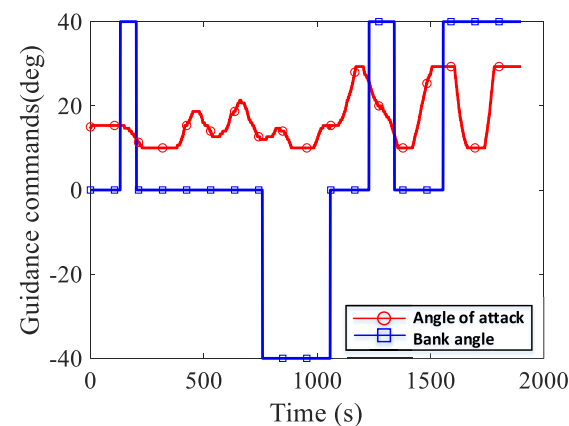**FIGURE 14.** Control commands for rectangular no-fly zone.



**FIGURE 16.** Control commands for sinusoidal channel no-fly zone.

constraint. Early in the flight, the middle tentacle touched the no-fly zone constraint and stop itself, whereas the other tentacles meet the other constraints and the two side tentacles are axially symmetric. As the vehicle flies ahead, the left tentacle meets the no-fly zone earlier than right tentacle, and this time the right one is selected. Then, during the middle period time, the left and middle tentacles meet the no-fly zones until the middle tentacle flies out of the no-fly zone. Next, the three tentacles of the vehicle break themselves just because of the constraints without a no-fly zone, whereas the left tentacle has closer break points from the end place. Finally, after a short flight to the left, the vehicle will head toward the end zone and will no longer maneuver left and right without a no-fly zone.

Figs. 13–16 show guidance commands for missions 1–4. The time-counting filter plays an important role in reducing control command oscillations in missions 1–3, whereas mission 4 does not need the filter. In missions 1–4, when there is nothing in front of the vehicle, the method used in [26] results in more bank reverse flying to the target. The advantages of three tentacles in the current study are more obvious in mission 3.

Note that the guidance method is not applicable to some kinds of no-fly zones when the three tentacles meet no-fly zones all along the flight, such as in a particularly narrow passageway or when there are big obstacles beyond the maneuverability of the vehicle.

### B. DISPERSED CASES FOR STATIC NO-FLY ZONE
To verify the robustness of the guidance strategy, dispersions of the initial conditions and some parameters are considered. The dispersions of the initial state are summarized in Table 1, and three times the standard deviation for dispersions of the lift coefficient, the drag coefficient, the aerodynamics density, and the vehicle mass are 5%, 5%, 15%, and 5%, respectively, with respect to their reference values. Particularly, the dispersions of the initial latitude and heading angle are more than the dispersions in [26]. The simulations are conducted for missions 1–4 by the Monte Carlo method under these dispersions and 1,000 trajectories are conducted in each mission.

The ground tracks of dispersed cases for mission 1-4 are the blue solid trajectories shown in Figs. 17–20, and the starting points of the ground tracks exhibit significant dispersion.
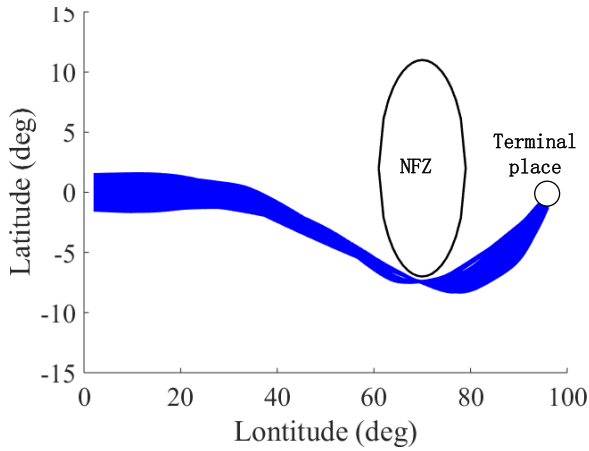
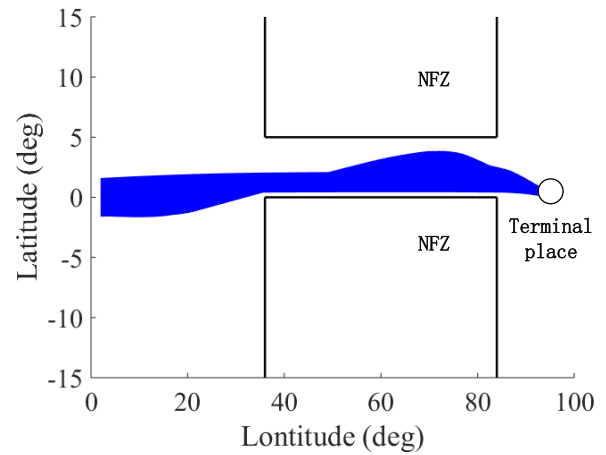**FIGURE 17.** Ground tracks for static circle no-fly zone in dispersed cases.



**FIGURE 18.** Ground tracks for static rectangle no-fly zone in dispersed cases.



**FIGURE 19.** Ground tracks for static double rectangular channel no-fly zone in dispersed cases.
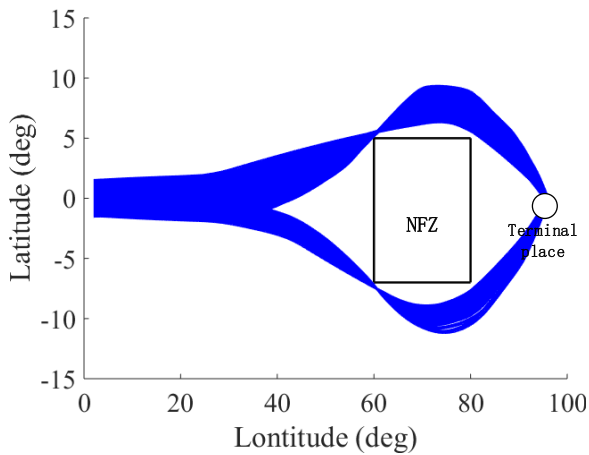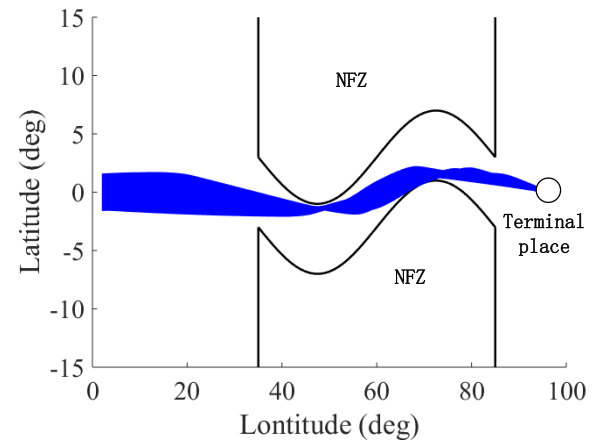


**FIGURE 20.** Ground tracks for static sinusoidal channel no-fly zone in dispersed cases.

However, the vehicle reached the terminal place successfully without meeting no-fly zones. It is clear from Figs. 17-20 that the vehicle tries to plan the shorter trajectories from the edges of no-fly zones to the terminal places. The vehicle chose the right side of the rectangular no-fly zone in Fig. 18 because the initial points of the vehicle slightly to the right of the central axis of the rectangle no-fly zone and the right side is more suitable for avoiding the no-fly zone.

### C. SIMULATION FOR DYNAMIC NO-FLY ZONES CASES

This section describes the feasibility of the guidance strategy for cases of dynamic no-fly zones. In this study, it is assumed that the speed in the no-fly zone still points toward the vehicle during the flight to make avoidance by the vehicle more difficult. In mission 5, the radius of no-fly zone is 1.5 deg and the velocity is 0.0075 deg/s, that is, 1394 km and 834.8 m/s. The vehicle reaches the terminal place with avoidance of a dynamic no-fly zone, as shown in Fig. 21, and the vehicle barely evades the no-fly zone approaching the vehicle. To confirm the influence of different initial places and different

velocities of dynamic no-fly zones, the simulation of three groups of control variables is carried out.

First, ten cases with linearly selected initial positions of no-fly zones are considered and these cases have the same velocity, 0.0075 deg/s, whereas the distances to the centers of the dynamic no-fly zones are shown in Fig. 22. With the distance between the no-fly zone and the starting point of the vehicle gradually increasing at the initial moment, the minimum value of ten curves only gradually increases from the left. The gradient colored lines plotted in Fig. 22 shows that the closer the vehicle is to the initial position of a dynamic no-fly zone, the harder it is to avoid the no-fly zone. If the initial position of the no-fly zone is further than 64 deg, the minimum distance from the vehicle to the center of the no-fly zone would be basically invariant, and the different initial positions has no effect on the avoidance.

Secondly, 10 cases with linearly selected velocities of no-fly zones are considered, and these cases have the same initial position of [60, 0] in longitude and latitude plane.
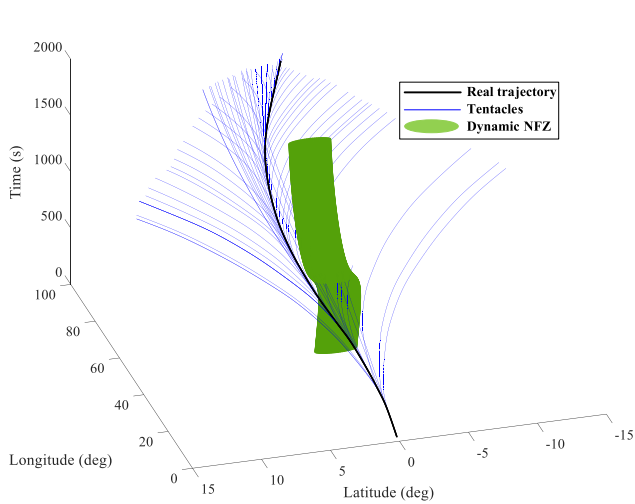
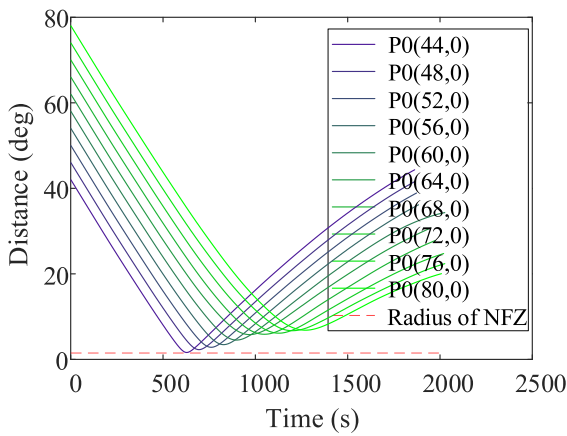**FIGURE 21.** Ground tracks changing with time for dynamic no-fly zone.



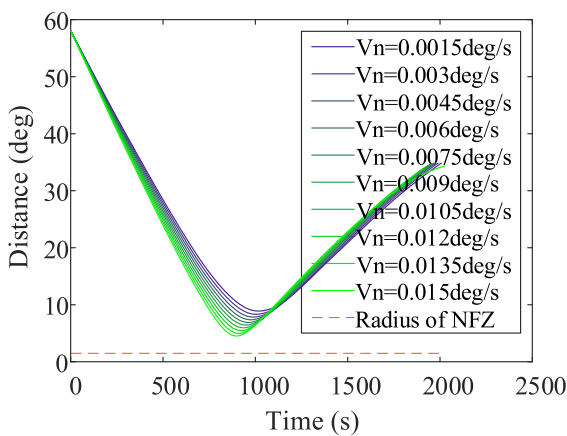**FIGURE 22.** Distance to dynamic no-fly zone with different initial places.



**FIGURE 23.** Distance to dynamic no-fly zone with different no-fly zone's velocity.

The results shown in Fig. 23 demonstrate that the faster the no-fly zone is, the harder it is for the vehicle to avoid the no-fly zone. In Fig. 22 and Fig. 23, each of the twenty distance results between the vehicle and the no-fly zone decreases to
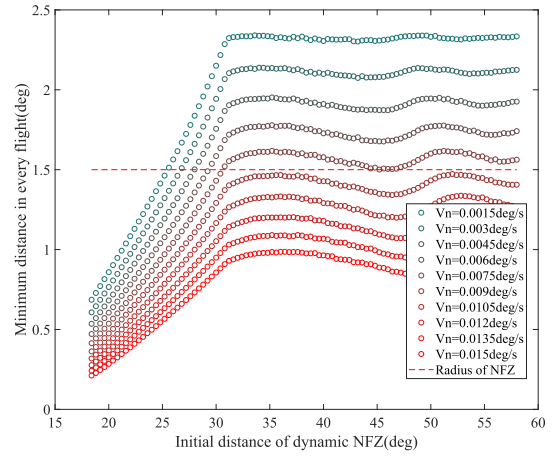


**FIGURE 24.** Minimum distance to dynamic no-fly zone with different initial place and velocity.
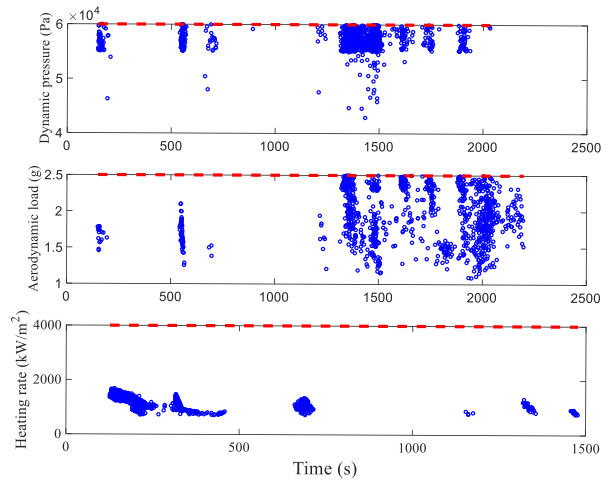


**FIGURE 25.** Path constraints for static mission 1 in dispersed cases.

the minimum at first and then increases, which shows that vehicle is in the process of avoiding the no-fly zone when the no-fly zone is closer to the nearest distance; the vehicle gradually escapes.

Finally, the dual effects of different speeds and different initial positions of dynamic no-fly zones are considered by combining 100 linearly selected initial positions and 10 linearly selected speeds into 1000 experiments for simulation, and the results are shown in Fig. 24. The simulation results in Fig. 24 show that the linearly selected initial positions have an effect when the distance between the vehicle and the no-fly zone is less than about 31 deg. However, the different velocities have a significant impact on the avoidance. Only when the velocity is less than 0.075 deg/s would the vehicle have an opportunity to avoid the dynamic no-fly zone.

### D. PATH CONSTRAINTS AND COMPUTATIONAL PERFORMANCE

Model validity and path constraint satisfaction are confirmed as shown in Figs. 25–32. The path constraints include dynamic pressure, aerodynamic load, and heating rate, which
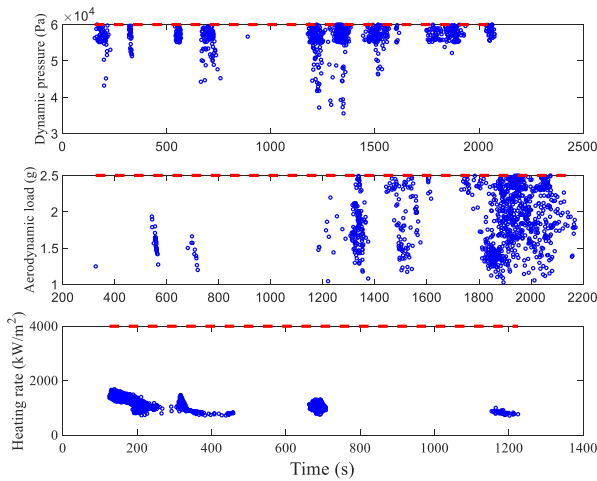
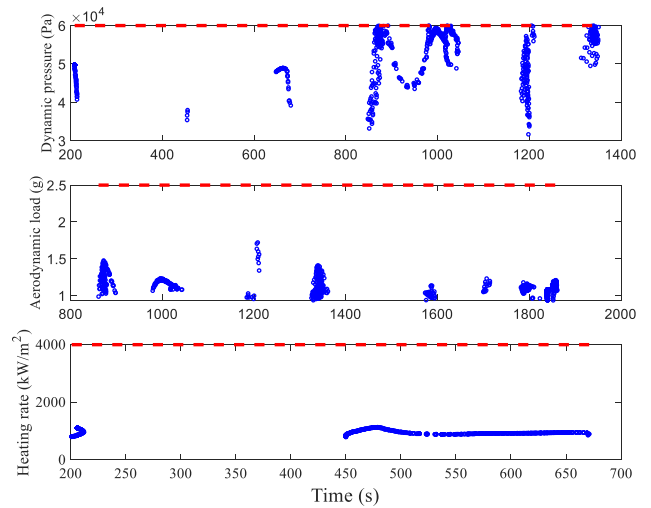**FIGURE 26.** Path constraints for static mission 2 in dispersed cases.
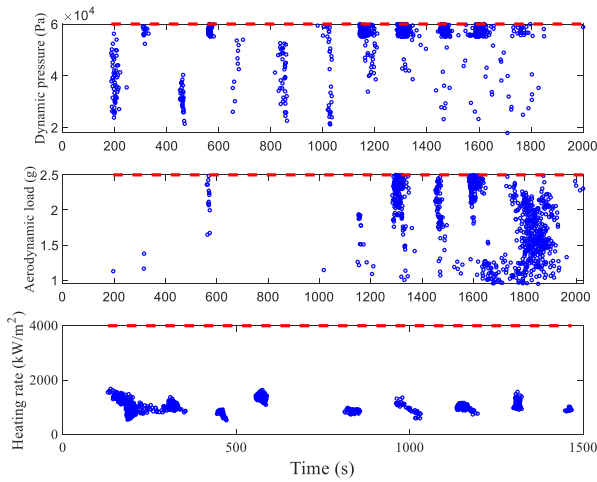


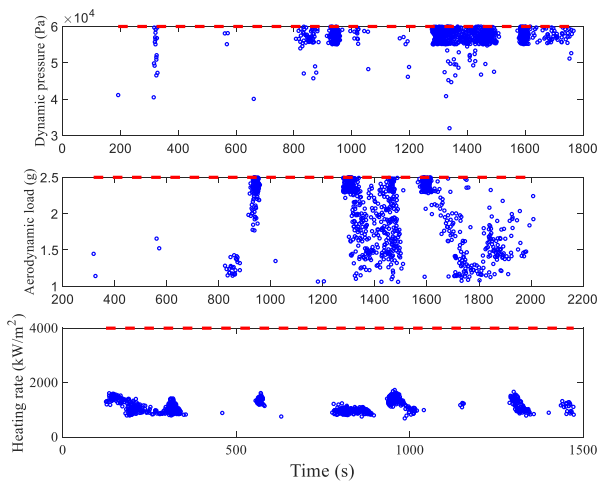**FIGURE 27.** Path constraints for static mission 3 in dispersed cases.



**FIGURE 28.** Path constraints for static mission 4 in dispersed cases.

are shown in Figs. 25–29. Figs. 25-28 are confirmed for static missions 1–4, whereas Fig. 29 is confirmed for the 1000 dynamic dispersion cases. Figs. 25–29 show that
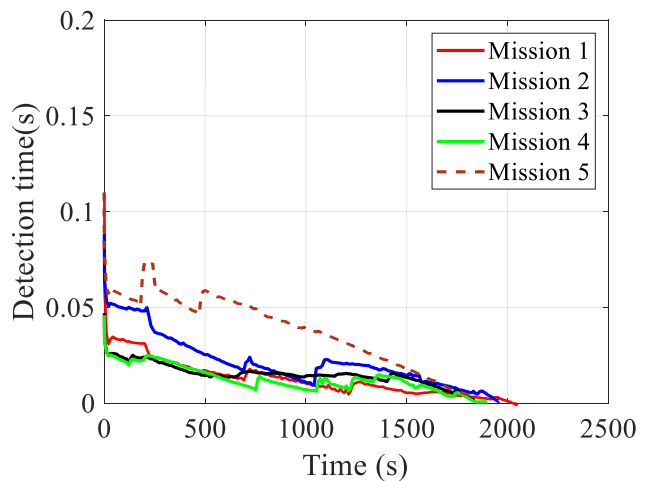


**FIGURE 29.** Path constraints for dynamic no-fly zones in dispersed cases.



**FIGURE 30.** Calculating time per cycle for no-fly zone missions 1-5.

the bank angle transient strategy based on the improved tentacle-detection method can still ensure the flight of the vehicle to meet these path constraints in the process of guidance, demonstrating that the vehicle can effectively track the standard trajectory in the discrete Monte-Carlo experiments. In theory, this improved tentacle-based method will not consume too much time [26]. The calculation performance of the method can be measured by the maximum, minimum, and average values of the calculation time of all the guidance periods in the different tasks. The simulation of the method was done on a mobile computer (CPU: 2.6GHz) using MAT-LAB software. Fig. 30 shows the calculation time in each detection cycle for missions 1–5. The method consumes more time at first, but the consuming time decreases in subsequent missions. Most of tentacles at the beginning are longer than those generated later. Therefore, the closer the vehicle is to the no-fly zone, the shorter the tentacles are and the less the detection time is.
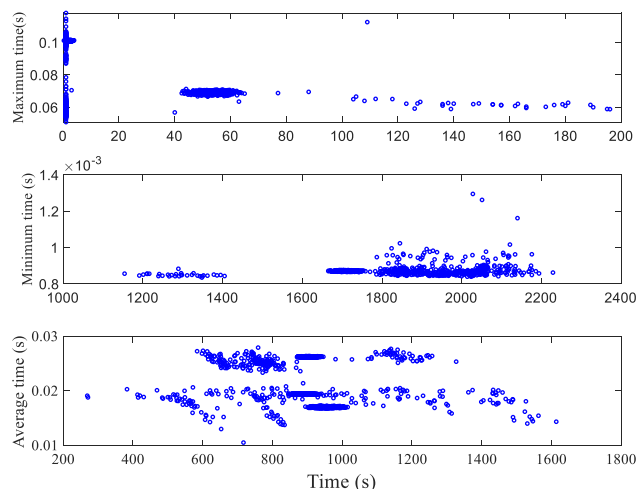
**FIGURE 31.** Detection time for static no-fly zone missions 1-4 in dispersed cases.
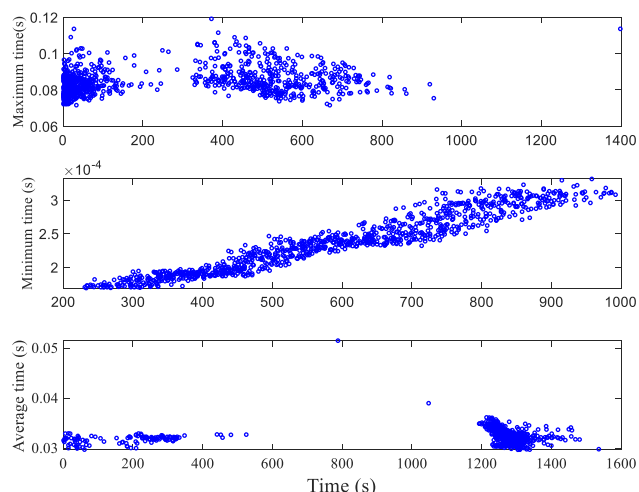


**FIGURE 32.** Calculating time for dispersed cases with dynamic no-fly zone.

The detection time is calculated and recorded in every cycle with the moment of the cycle, and the maximum and minimum detection times are found, whereas their moments in the flight are recorded separately. As for the average detection time, calculated after the whole flight, the moment is found in the flight when the detection time is the closest to average detection time; the moment is then recorded. The moments above are the *X* coordinate in Fig. 31 and Fig. 32. As shown in the two figures, the maximum computation times are less than 0.15 s, so the minimum computation time is in milliseconds and the average computation time is on the order of $10^{-2}$ s. All these results show that this improved tentacle-based guidance strategy can be used online in the maneuvering guidance.

## V. CONCLUSION

A bank angle transient guidance strategy based on improved tentacles is proposed for the reentry of hypersonic vehicles to avoid no-fly zones. Compared to the guidance strategy in the

cases of no-fly zones with prior known information, this strategy is not dependent on the all the information of the no-fly zone; it is only dependent on the three detection tentacles' feedback to give control commands, and the results show that the method has a good applicability for both static and dynamic no-fly zones. In the guidance process, the heading angle constraint and the warning area of the dynamic no-fly zone are put forward, which improves the maneuvering of the vehicle to avoid different types of no-fly zones. In addition, only three tentacles are generated in each guidance cycle, which ensures the rapidity of calculation. Further, regarding the control commands of the vehicle, there are only three control commands for lateral maneuver guidance with less variation times conducted by time-counting filter. Finally, if the information of the dynamic no-fly zone could be effectively identified through reinforcement learning, the avoidance of the vehicle will be better. Such improvement will be considered in further studies.

## REFERENCES

[1] J. C. Harpold and C. A. Graves, Jr., "Shuttle entry guidance," *J. Astronaut. Sci.*, vol. 27, no. 3, pp. 239–268, Jul. 1979.

[2] P. Lu, "Trajectory optimization and guidance for a hypersonic vehicle," in *Proc. 29th AIAA Aerosp. Sci. Meeting*, 1991, p. 5068.

[3] W. Grimm, "On ascent guidance of a hypersonic vehicle," *IFAC Autom. Control Aerosp.*, pp. 496–500, 1992.

[4] P. Lu, J. M. Hanson, D. Bose, R. Beck, and B. Strovers, "Entry guidance for the X-33 vehicle," *J. Spacecraft Rockets*, vol. 35, no. 3, pp. 342–349, 1998.

[5] C. Bahm, E. Baumann, J. Martin, D. Bose, R. Beck, and B. Strovers, "The X-43A hyper-X mach 7 flight 2 guidance, navigation, and control overview and flight test results," in *Proc. AIAA/CIRA 13th Int. Space Planes Hypersonics Syst. Technol. Conf.*, Capua, Italy, 2005, p. 3275.

[6] P. Lu, D. B. Doman, and J. D. Schierman, "Adaptive terminal guidance for hypervelocity impact in specified direction," *J. Guid., Control, Dyn.*, vol. 29, no. 2, pp. 269–278, Mar. 2006.

[7] J. Benito and K. D. Mease, "Reachable and controllable sets for planetary entry and landing," *J. Guid., Control, Dyn.*, vol. 33, no. 3, pp. 641–654, 2010.

[8] M. Sayadi, A. Kosari, and P. M. Zadeh, "Robust optimal control for precision improvement of guided gliding vehicle positioning," *IEEE Access*, vol. 6, no. 1, pp. 25797–25815, 2018.

[9] H. X. Zhang, Z. F. Gong, and G. B. Cai, "Reentry tracking control of hypersonic vehicle with complicated constraints," *J. Ordnance Equip. Eng.*, vol. 40, no. 1, pp. 1–6, 2019.

[10] R. Wang, S. Tang, and D. Zhang, "Short-range reentry guidance with impact angle and impact velocity constraints for hypersonic gliding reentry vehicle," *IEEE Access*, vol. 7, pp. 47437–47450, 2019.

[11] Y. Gao, G. B. Cai, and S. X. Zhang, "Reentry maneuver guidance for hypersonic glide vehicles under multiple no-fly zones," *J. Ordnance Equip. Eng.*, to be published.

[12] G. T. Huntington, D. Benson, and A. V. Rao, "A comparison of accuracy and computational efficiency of three pseudospectral methods," in *Proc. AIAA Guid., Navigat. Control Conf. Exhib.*, Hilton Head, SC, USA, 2007, p. 6405.

[13] Q. Gong, F. Fahroo, and I. M. Ross, "Spectral algorithm for pseudospectral methods in optimal control," *J. Guid., Control, Dyn.*, vol. 31, no. 3, pp. 460–471, May 2008.

[14] C. L. Darby, W. W. Hager, and A. V. Rao, "An hp-adaptive pseudospectral method for solving optimal control problems," *Optim. Control Appl. Methods*, vol. 32, no. 4, pp. 476–502, 2011.

[15] X. X. Cheng, H. Li, R. Zhang, and Z. Zhang, "Efficient trajectory planning for solid rocket-powered launch vehicles based on the Newton-kantorovich/pseudospectral approach," in *Proc. 21st AIAA Int. Space Planes Hypersonics Technol. Conf.*, Xiamen, China, 2017, p. 2231.

[16] Z. Jin, S. Lei, W. Huaji, Z. Dayuan, and L. Humin, "Optimal midcourse trajectory planning considering the capture region," *J. Syst. Eng. Electron.*, vol. 29, no. 3, pp. 147–160, 2018.

[17] A. J. Roenneke and A. Markl, "Re-entry control to a drag-vs-energy profile," *J. Guid., Control, Dyn.*, vol. 17, no. 5, pp. 916–920, Sep. 1994.

[18] E. M. Yong, G. J. Tang, and L. Chen, "Rapid trajectory planning for hypersonic unpowered long-range reentry vehicles with multi-constraints," *J. Astronaut.*, vol. 29, no. 1, pp. 46–52, Jan. 2008.

[19] J. A. Leavitt and K. D. Mease, "Feasible trajectory generation for atmospheric entry guidance," *J. Guid., Control, Dyn.*, vol. 30, no. 2, pp. 473–481, 2007.

[20] Z. X. Liang, Z. Ren, and Q. D. Li, "Evolved atmospheric entry corridor with safety factor," *Acta Astron.*, vol. 143, no. 1, pp. 82–91, 2018.

[21] T. R. Jorris and R. G. Cobb, "Three-dimensional trajectory optimization satisfying waypoint and no-fly zone constraints," *J. Guid., Control, Dyn.*, vol. 32, no. 2, pp. 551–572, 2009.

[22] Z. X. Liang, Q. D. Li, and Z. Ren, "Waypoint constrained guidance for entry vehicles," *Aerosp. Sci. Technol.*, vol. 52, no. 1, pp. 52–61, 2016.

[23] F. von Hundelshausen, M. Himmelsbach, F. Hecker, A. Mueller, and H.-J. Wuensche, "Driving with tentacles: Integral structures for sensing and motion," *J. Field Robot.*, vol. 25, no. 9, pp. 640–673, 2008.

[24] A. Cherubini, F. Spindler, and F. Chaumette, "Autonomous visual navigation and laser-based moving obstacle avoidance," *IEEE Trans. Intell. Transp. Syst.*, vol. 15, no. 5, pp. 2101–2110, Oct. 2014.

[25] A. Cherubini, F. Spindler, and F. Chaumette, "A new tentacles-based technique for avoiding obstacles during visual navigation," in *Proc. IEEE Int. Conf. Robot. Autom.*, Saint Paul, MN, USA, May 2012, pp. 4850–4855.

[26] Z. X. Liang and Z. Ren, "Tentacle-based guidance for entry flight with no-fly zone constraint," *J. Guid., Control, Dyn.*, vol. 41, no. 4, pp. 991–1000, Apr. 2018.

[27] G. Williams, A. Aldrich, and E. A. Theodorou, "Model predictive path integral control: From theory to parallel computation," *J. Guid., Control, Dyn.*, vol. 40, no. 2, pp. 344–357, 2017.

[28] N. X. Vinh, A. Busemann, and R. D. Culp, "Hypersonic and planetary entry flight mechanics," Univ. Michigan, Ann Arbor, MI, USA, Tech. Rep., 1980.

[29] D. R. Chapman, "An approximate analytical method for studying entry into planetary atmospheres," NASA, Washington, DC, USA, Tech. Rep. NASA TR R.11, 1959.

[30] G. Dukeman, "Profile-following entry guidance using linear quadratic regulator theory," in *Proc. AIAA Guid., Navigat., Control Conf. Exhib.*, Monterey, CA, USA, Jun. 2002, p. 4457. [Online]. Available: https://arc.aiaa.org/doi/abs/10.2514/6.2002-4457

[31] Z. J. Shen and P. Lu, "Onboard generation of three-dimensional constrained entry trajectories," *J. Guid., Control, Dyn.*, vol. 26, no. 1, pp. 111–121, Jan. 2003.

[32] P. Lu, "Entry Guidance: A unified method," *J. Guid., Control, Dyn.*, vol. 37, no. 3, pp. 713–728, Feb. 2014.

[33] P. Lu, C. W. Brunner, G. F. Mendeck, M. Tigges, and C. Cerimele, "Verification of a fully numerical entry guidance algorithm," *J. Guid., Control, Dyn.*, vol. 40, no. 2, pp. 230–247, Feb. 2017.

[34] T. H. Phillips, "A common aero vehicle (CAV) model, description, and employment guide," Schafer Corp. Air Force Res. Lab., Air Force Space Command, Wright-Patterson Air Force Base, OH, USA, Tech. Rep., Jan. 2003.

**YANG GAO** received the B.S. degree from the Department of Control Engineering, Rocket Force University of Engineering, in 2017, where he is currently pursuing the M.S. degree in control science and engineering. His current research interests include maneuvering guidance of hypersonic vehicle and reinforcement learning.

**GUANGBIN CAI** received the Ph.D. degree in control science and engineering, Rocket Force University of Engineering, in 2012, where he is currently an Associate Professor with the College of Missile Engineering. His main research interests include guidance and control theory and its applications of aircrafts. He received the reward-gainer of the excellent doctor degree dissertation in Shaanxi, China.
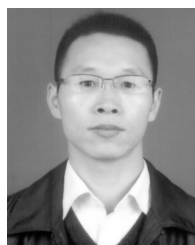
**XIAOGANG YANG** received the Ph.D. degree from the Control Engineering Department, Rocket Force University of Engineering, in 2006. He is currently a Professor and the Deputy Director of the Control Engineering Department, Rocket Force University of Engineering. His main research interests include precision guidance and image processing.

**MINGZHE HOU** received the Ph.D. degree in control science and engineering from the Harbin Institute of Technology, China, in 2011. From 2012 to 2016, he was a Lecturer with the Center for Control Theory and Guidance Technology, Harbin Institute of Technology, where he became an Associate Professor, in 2017. His main research interests include nonlinear control theory and its applications in guidance and control of aircrafts.

• • •